CHANDRA
X-ray Center

MEMORANDUM

March 1, 1999

File: /stage/brm/Acisdata/Xrcf/Psf/Memo/paper6.tex

To: CXC & ACIS team

From: A. Ware, B.R. McNamara

Subject: An Analysis of the ACIS-HRMA Point Response Function

Abstract

We have analyzed images of point-like X-ray sources obtained at the X-ray Calibration Facility (XRCF) in Huntsville, AL during the Phase H calibration period April 18–26, 1997. We describe the PRF using several methods, including the encircled energy radius, azimuthally averaged radial surface brightness profiles, radial surface brightness profiles in orthogonal, one pixel wide slices, and marginal surface brightness distributions. These spot profiles are often presented as a function of event grade distribution, which is particularly sensitive to photon event pileup. To assess and validate the Chandra telescope model, we performed identical analyses of SAOSAC+MARX simulations for several XRCF tests, and compared the results of the models directly to the XRCF data. The model included the effects of gravity, finite source distance, mirror misalignments, and the $\sim 10\%$ decrease in the mirror effective area discovered during the HRMA Phase F calibration. The model included the additional effects of finite source size for the on-axis PRF core measurement, but did not account for non-monochromaticity of the X-ray source. The ACIS+HRMA point response function (PRF) shows a complex dependence on the incident count rate, defocus, pixel size, detector geometry, and most importantly the HRMA (mirror) properties. The model is sharper than the XRCF on-axis data by $\sim 7\%$ in the on axis FWHM and $\sim 3\%$ in the 70% encircled energy radius. The accuracy of this comparison is limited by unmodeled CCD pixelation effects. The off-axis model spot beyond four arcminutes is sharper in the 70% encircled energy radius compared to the XRCF spot by only $\lesssim 10\%$, and the rate of growth of the model and XRCF spots with increasing off-axis angle agree to within the measurement errors. This Memorandum is intended as a brief summary of the detailed analyses and data products available on the web at `http://asc.harvard.edu/cal/Links/Acis/acis/Cal_prods/psf/psf.html`.

1 Data Analysis Plan

Our goal is to validate the CXC's telescope model to ensure that the on-orbit PRF can be reliably modeled at any axial location and for arbitrary source spectral energy distribution. Our analysis strategy is shown schematically in Figure 1. The parameters for each test, defined by its TRW identification code, are taken from the so-called as run Calibration Measurement Data Base (CMDB). The parameters for each test drawn from the CMDB (e.g. ACIS mode, axial location, defocus position, etc.) served as boundary conditions to SAOSAC+MARX models. The SAOSAC raytrace included corrections for gravity ovalization, finite source distance geometry, mirror misalignments, and the $\sim 10\%$ reduction in effective area discovered during Phase F. The ACIS model is a simple "slab-and-stop" detector model capable of treating charge spreading between pixels, but does not include a detailed treatment of the sub-pixel structure on the front illuminated (FI) devices, nor does it include a back illuminated (BI) model device. The "Analysis" box lists the analysis methods applied identically to both XRCF and model images and spectra (we discuss each in detail below). When the data and model analyses disagreed, certain model parameters were adjusted in an attempt to attain agreement between the model and data. The model can be applied to on-orbit imaging by removing the compensation for ground effects from the model. We intend to repeat this validation procedure using on-orbit data.

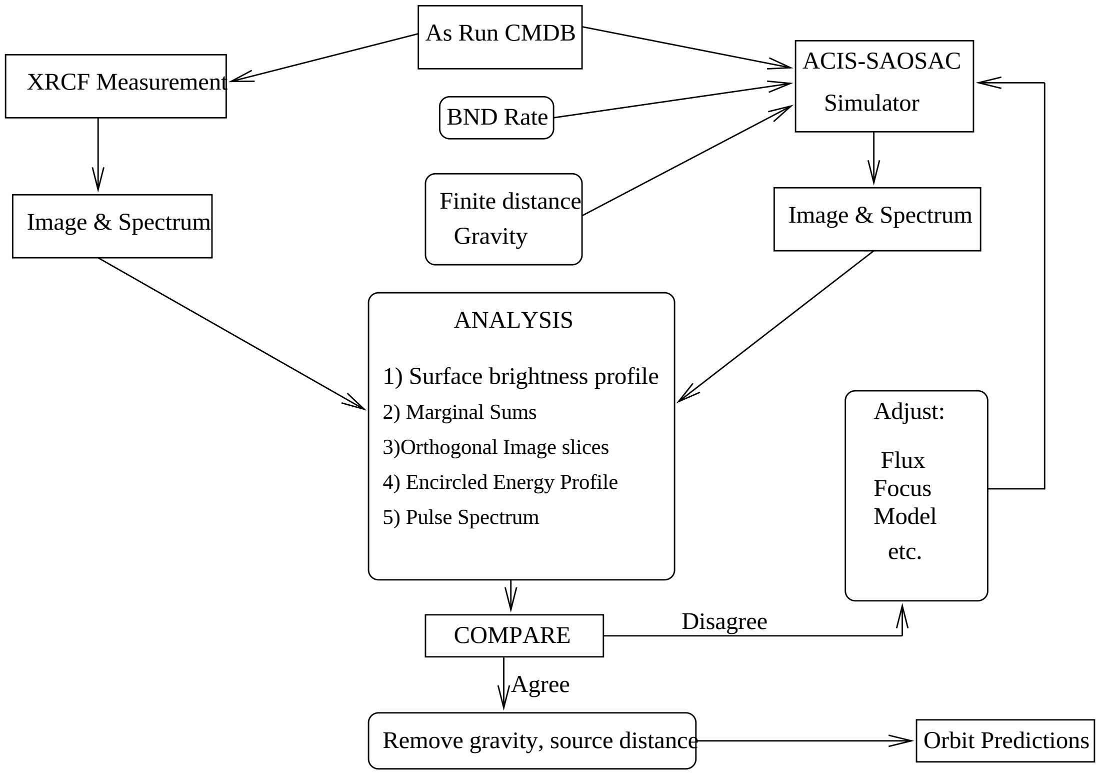

Figure 1: Schematic of data analysis strategy.

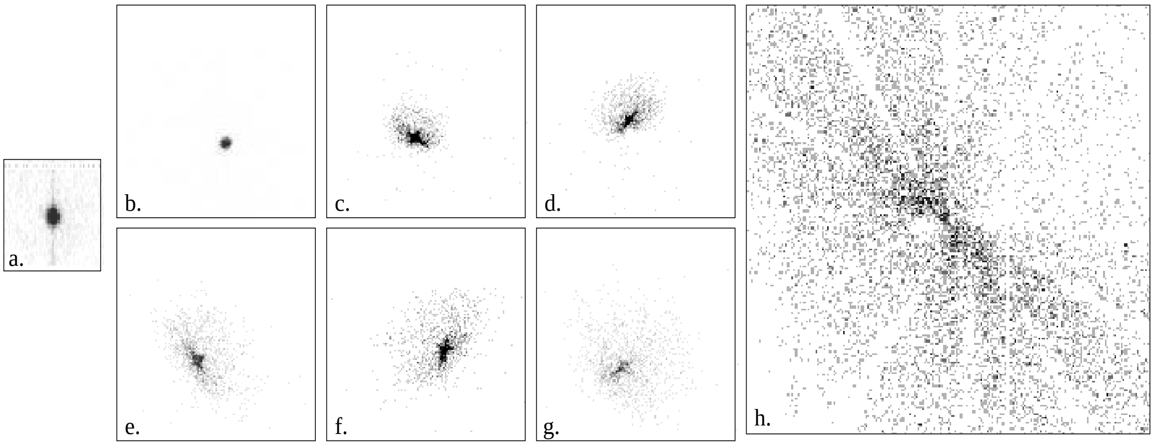

Figure 2: Change in the PRF shape with angular distance from the optical axis as viewed at the XRCF. Off-axis angle in arcmin: a) 0, b) 1.69, c) 7.57, d) 8.67, e) 10.57, f) 11.46, g) 12.27. Image h) is an ACIS-S image and is 27.20 arcmin off-axis.

2 ACIS Data Acquisition Modes

Most of the analysis was performed on data acquired with the ACIS high speed data tap implemented at the XRCF. This mode of data acquisition allowed, in principle, each CCD readout frame to be processed and archived from one of the 10 ACIS devices. The "tapped" device was usually illuminated by the focussed X-ray spot. The measurements discussed here were obtained in timed event (TE) mode and staggered readout mode. These modes expose the CCDs to focussed X-rays in subarrays whose sizes depend on the duration of the subarray exposure or frametime (see Table 1). Because the spot size is a strong function of axial location, the subarray size (frametime) was adjusted to accommodate the spot, as is shown to proper scale in Figure 2. Typical subarray sizes and frametimes are given in Table 1.

The staggered readout mode shifts a specified number of rows into the framestore region while exposing the remaining frame to X-rays while the subframe is processed through the detector electronics. This mode results in a 1024 pixel full-frame image with a series of X-ray spots located on each subframe. The number of spots per full frame is 1024 divided by the number of rows per staggered readout frame. In order to analyze the images, the subframes were extracted from the HST full frame images and added to form a single, high signal-to-noise subframe. An example of a staggered readout frame is shown in Figure 3. The short frametime capability of the staggered array mode significantly boosted the photon collection efficiency by providing for high source fluxes with minimal pileup. Its primary disadvantage is that it exposes each subframe to X-rays over the entire readout time of the full CCD frame, resulting in a higher background. For this reason, only the core of the spot was studied using this mode. Staggered readout mode is not an option in-flight. The subarray TE mode CCD frames were likewise added to form a high signal-to-noise images.

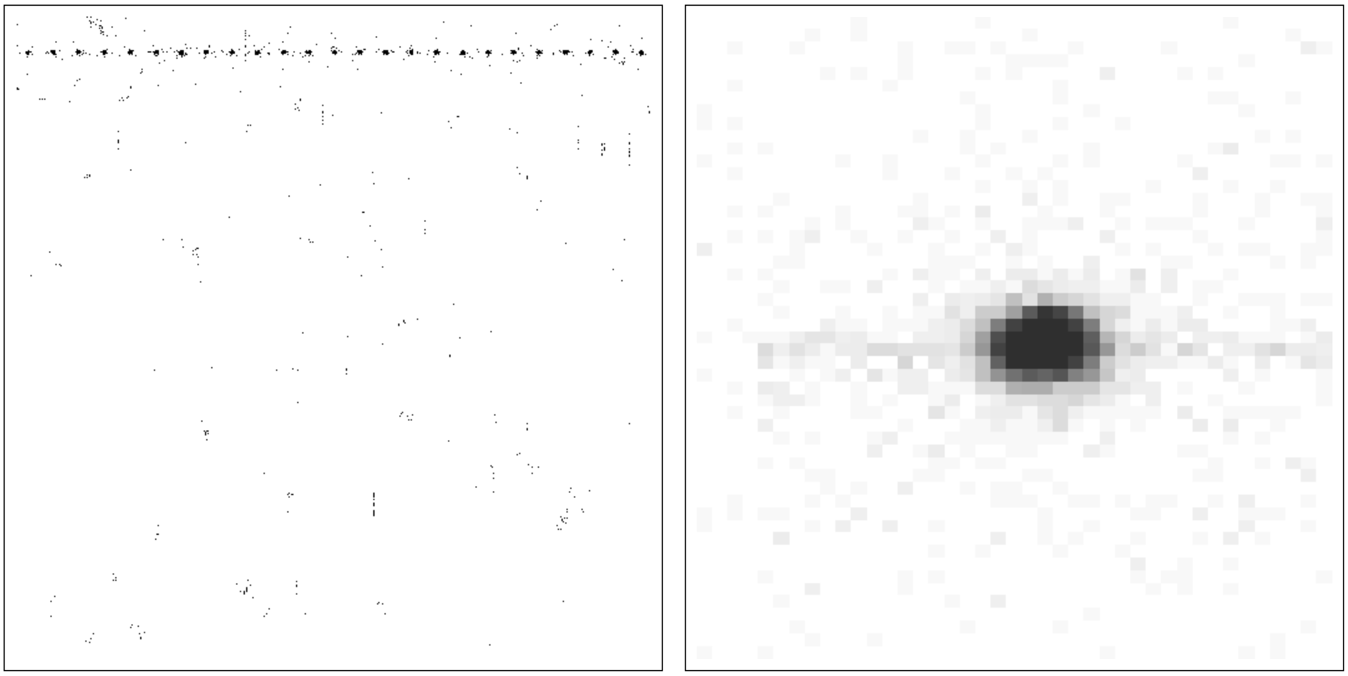

Figure 3: H-IAI-CR-1.005. Left: Staggered readout mode image. Right: Staggered rows stacked to form a single image (magnified).

3 High Speed Tap Data Reduction

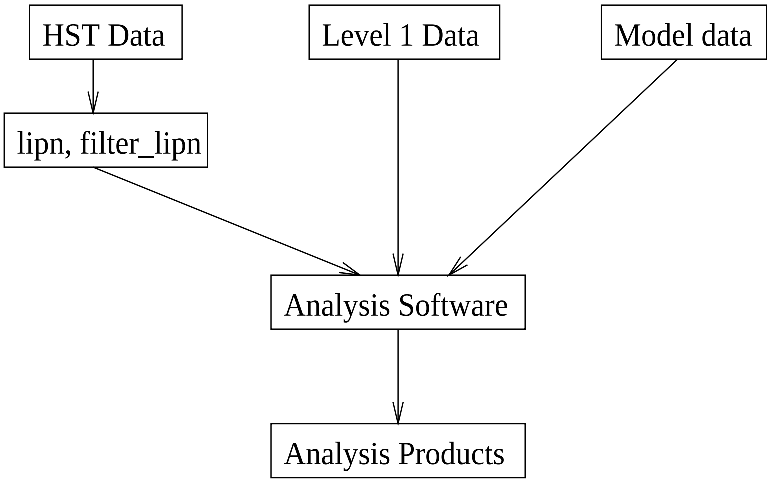

Figure 4: Schematic of data reduction and analysis procedure.

A schematic view of our analysis procedure is shown in Figure 4. The science CCD frames and bias maps were processed using event detection and analysis software similar to that used during the laboratory calibration at MIT. (Level 1 telemetry event lists were analyzed for several off-axis measurements whose HST data became corrupted.) The event detection software used an event threshold of 50 ADU and a split threshold of 20 ADU. K. Glotfelty's `lipn` and `filter_lipn` software packages were used to combine the event lists for each test into images and pulse height spectra.
(see `http://hea-www.harvard.edu/acis/software/software.html`)

Table 1: Subframe Sizes and Exposure times

Frametime (seconds)	Number of rows
0.122	38
0.5	100
0.8	256
3.3	1024

4 Data Analysis

We developed a set of IDL procedures to generate the analysis products discussed below. Examples of the methods summarized here are shown in Figure 5.

- *Radial Surface Brightness Profiles:* computed by summing the X-ray events in annuli centered on the image, and dividing by the respective area of each annulus.
- *Cumulative Radial Distributions (Encircled events):* computed by summing the X-ray events within centered circular apertures of increasing radius, and normalizing the distribution to the total number of counts within a radius of 1.6 mm. Note that the central pixel is defined as 1 in our encircled counts plots (e.g. Figures 5, 14, 19).
- *Marginal Distributions:* computed as $M(y) = \sum_{\text{events}} z dy$ and $M(z) = \sum_{\text{events}} y dz$ in rectangular grids surrounding the X-ray spot.
- *Orthogonal Image Slices:* computed by extracting the the X-ray events along the CCD row and column that intersects the spot centroid, and dividing by the pixel area.
- *Pulse Height (PH) Spectra:* The charge in each 3×3 pixel event island was summed, after removing the bias charge from each pixel, and the histogram of pulse heights was plotted. Because the incident X-rays were nearly monochromatic with known energies, it was not necessary to apply a gain correction.

These methods of presenting the data were chosen for their sensitivity to distortions in the spot size and shape resulting from mirror nonparfocalization, telescope defocus (x-direction), scattering, photon event pileup, finite pixel size, and detector geometry.

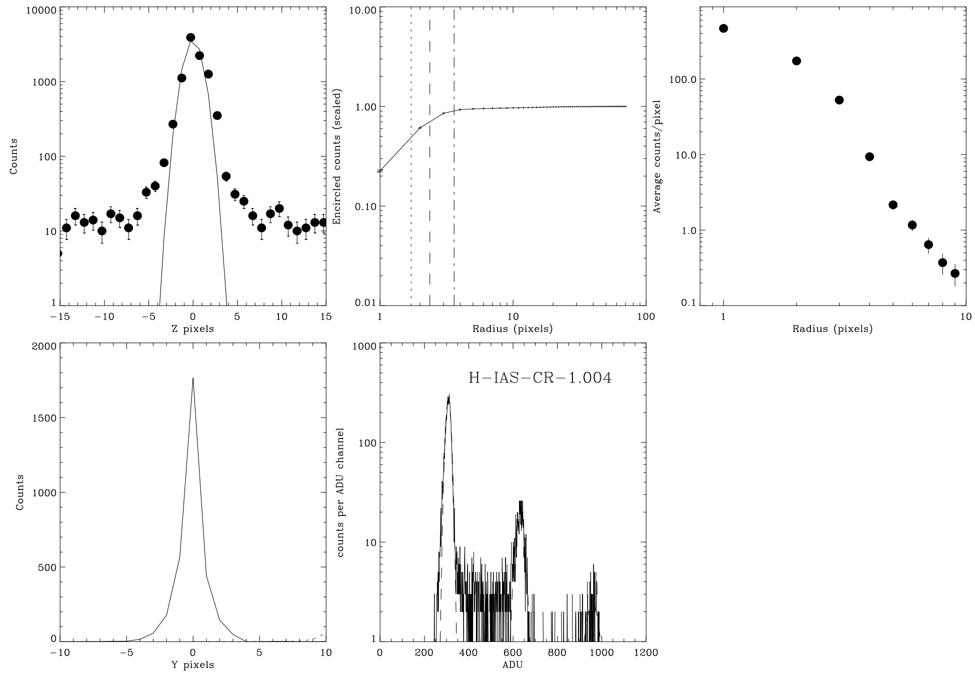

Figure 5: Examples of analysis products. Top row: marginal distribution (Z direction), encircled energy, and radial profile for H-IAI-CR-1.001. Bottom row: one-pixel-wide slice (Y direction) for H-IAI-CR-1.001 and pulse height spectrum showing pileup peaks for H-IAI-CR-1.004.

5 The On-axis Point Response Function

5.1 The Core of the Point Response Function

In Figures 6 and 7 we plot the marginal distribution and slices for an image of an Al-K 1.486 keV anode spot. This image was obtained in staggered readout mode (e.g. Figure 3, test H-IAI-CR-1.001), and has the lowest count rate per frame ($\simeq$ 0.2 photons per frame), hence the lowest degree of pileup among the ACIS measurements obtained at the XRCF. It should, in principle, have the smallest ACIS spot size obtained at the XRCF. The spot shows obvious asymmetries in shape, and it is broader along the Z axis than along the Y axis. The Z axis is parallel to the gravity vector and the Y axis is parallel to the CCD readout direction. The direction of the readout can be seen by the trail across the summed image shown in Figure 3.

The asymmetries in Figures 3 and 5 are similar to those seen in the two dimensional scan data for the ensemble HRMA (C-IXF-P2-2.001) obtained during XRCF Phase C with a proportional counter and 10 μm diameter pinholes rastered on 10 μm centers (see NAS8-40224), effectively $\sim 10\mu$m pixels. By comparison, the ACIS images have 24 μm pixels, and thus have less than half the sampling of the scan data. The full width at half maximum (FWHM) of the Al-K scan data are $\mathrm{FW_y(s)} = 22.6$ μm and $\mathrm{FW_z(s)} = 25.3$ μm (NAS8-40224, Table 4.4), whereas we find $\mathrm{FW_y(A)} = 47$ μm and $\mathrm{FW_z(A)} = 65$ μm for the ACIS measurements. The increased spot size of the ACIS data compared to the scan data is consistent with the decreased sampling of ACIS, or "pixelization." The larger width of the spot in the Z direction seen in both data sets is likely to be residual gravity ovalization. However, the origin of the asymmetries in the ACIS spot stem from the HRMA optics,

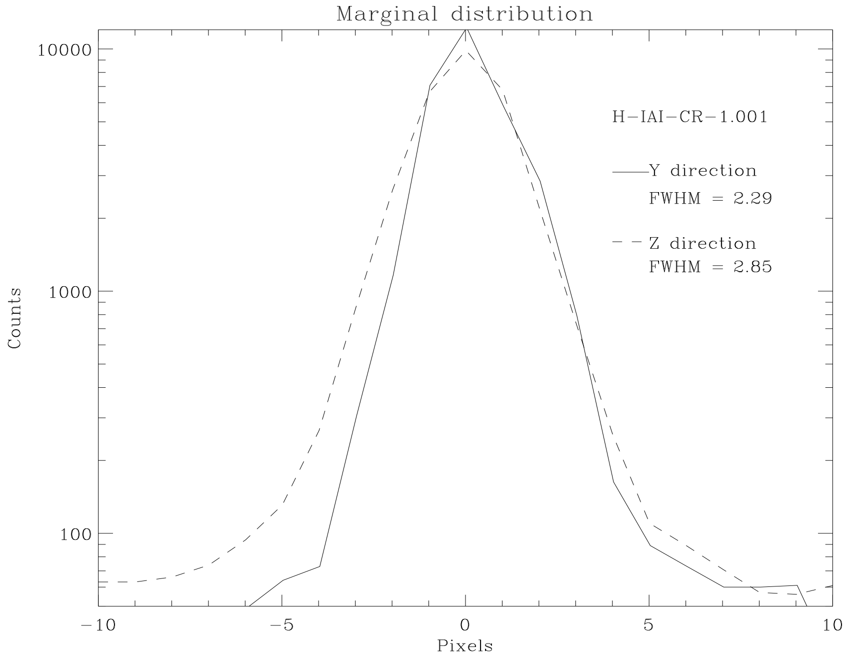

Figure 6: Marginal distribution in Y and Z directions for image H-IAI-CR-1.001, demonstrating gravity ovalization effects.

rather than sampling, because the asymmetries, particularly along the Y axis, are seen in both data sets. The 70% encircled energy radii for the ACIS and scan data are 55 μm and 75 μm respectively. The difference in these figures can probably be explained by sampling.

In Figure 8 we examine the width of the on-axis spot as a function of energy for the tests listed in Table 23. Figure 8 shows the FWHMs of slice profiles along the Y axis, as in Figure 7. The FWHMs were measured by fitting Gaussians to the profiles. The top panel of Figure 8 includes all grade events and the bottom panel includes ASCA grades 0, 2, 3, 4, and 6 (G02346). Measurements in which the degree of photon pileup is less than 10% are shown as triangles, and those with pileup greater than 10% are shown as squares. The degree of pileup is unknown for the low-energy O-Kα data (crosses) because their pileup peaks were indistinguishable from other features in the spectra. Based on the X-ray fluxes, we expect pileup to be less than a few percent. The solid symbols represent measurement with the S3 backside CCD. This figure shows that the spot FWHM is, to the limits of precision, nearly independent of energy and event grade. In addition, the FWHM is not terribly sensitive to pileup for pileup fractions below $\sim$ 20%. The spot size measured with the backside device appears to be slightly smaller than the measurements obtained with the frontside device. This slight improvement may be due to the smoother surface of the backside device, a slightly improved focus, or some other explanation.

In Figure 9 we examine the properties of the cumulative distribution of counts or energy (we use counts, events, and energy interchangeably) as a function of spot size by plotting the on-axis 70% and 90% encircled energy radii as a function of energy for 20 tests listed in Table 23. The symbol definitions are the same as for Figure 8. The 70% encircled energy radius at Al-K is $\sim$ 2.3 pixels, whereas the 90% radius increases to about 3.8 pix. The 70% radius shows a weak dependence on energy. The 90% radius shows a pronounced gradient, increasing from 3.8 pixels to about 5.5 pixels at the 6.4 keV Fe-Kα feature, although the gradient is only marginally significant.

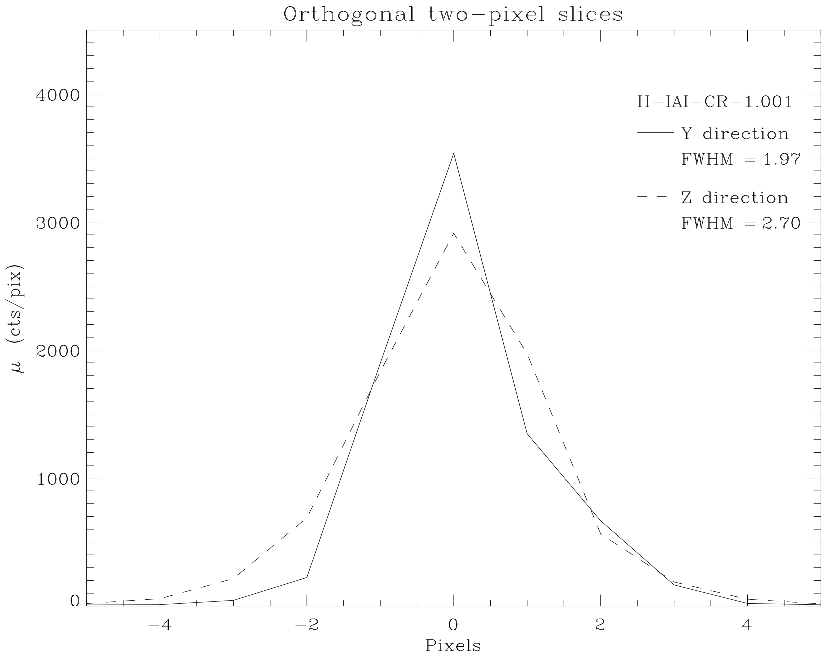

Figure 7: PSF shape: orthogonal slices through H-IAI-CR-1.001, showing the effects of gravity ovalization.

In the limit of zero energy, we find EER(70%)=2.28 pix and EER(90%)=3.43 pix. *We note again our definition of the central pixel as 1 for purposes of plotting the cumulative distributions on a logarithmic scale.* The actual 70% and 90% radii in pixels are 1.28 pixels and 2.43 pixels respectively.

Event pileup sharply increases the 70% and 90% EER, as shown in Figure 7. This is the result of lost events in the PRF's concentrated core relative to the wings. The EER is apparently more sensitive to pileup than the FWHM. A more exhaustive discussion of photon event pileup can be found in §7 and in
`http://asc.harvard.edu/cal/Links/Acis/acis/Cal_prods/pileup/pileup.html`

5.2 The Wings of the Point Response Function

The small, on-axis spot size adds a degree of difficulty to the study of the wings ($r \gtrsim 5$ arcsec), as only ~ 1 in 100 photons reach beyond a radius of 5 arcsec. High photon fluxes and azimuthal averaging are required to obtain a good signal. An example of a surface brightness profile for an Fe-Kα target is shown in Figure 10. The incident flux of Fe-Kα photons was roughly 250 counts per second (corrected for QE), and the frametime of 0.122 sec provided for a fluence of $\sim$ 30 counts per frame. At this rate the core of the spot is saturated, strong pileup occurs over the central several pixels, and the shape of the PRF is distorted.

Ten tests at several energies between $0.7 - 8$ keV were conducted to measure the wings of the PRF. Based on SAOSAC simulations, the azimuthally averaged, radial surface brightness profile is expected to decrease in the power law fashion $\mu(r, E) \sim r^{\alpha(E)}$. We therefore measured the power law index $\alpha(E)$ using least squares linear fits in log–log space to the surface brightness profiles of each image. The fit to the Fe-Kα $E = 6.4$ keV data for test H–IAS–PW–1.043 is shown in Figure 10 with the linear fit superposed. We find a power law

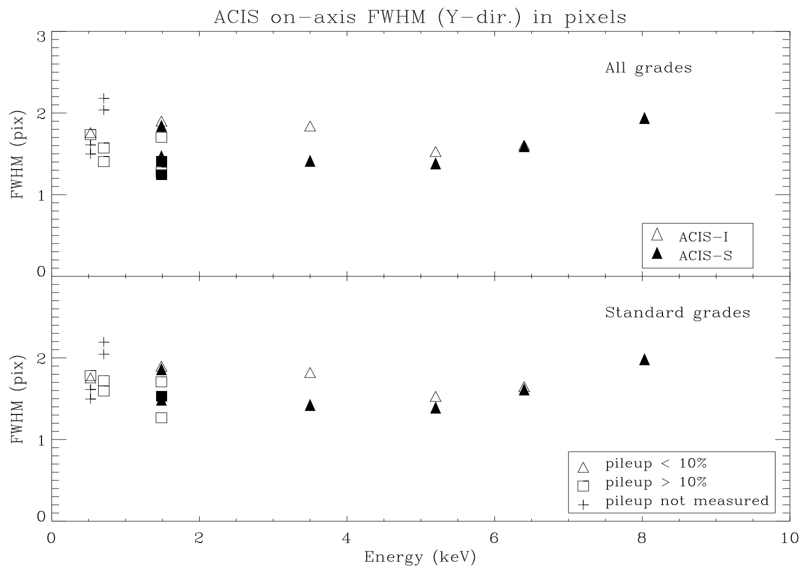

Figure 8: PSF shape: full width half max (in pixels) of Gaussian fits to orthogonal slices through the brightest pixel

profile of $\mu \sim r^{-1.3}$ between 10 and 15 pixels. The annular region between 10–15 pixels was chosen to avoid pileup in the inner region, and to avoid poor statistics at the edges of the subarrays where the density of events and the area are diminished.

A plot of power law index $\alpha(E)$ as a function of energy is shown in Figure 11. We find a smooth, quadratic increase in $\alpha(E)$ with increasing energy, indicating broadening wings and flattening profiles with increasing energy. This trend presumably reflects the increasing dominance of shell 6 with increasing energy.

6 The Off-Axis Point Response Function

PRF measurements were obtained at the XRCF at three energies and at several off-axis angles between $4 - 12$ arcmin with ACIS–I and $4 - 9$ arcmin with ACIS–S. The spot size growth with off-axis angle and energy is shown in Figure 12. The 70% encircled energy radii (EER(70%)) are shown as circles and the 90% encircled energy radii (EER(90%)) are shown as triangles. Filled points indicate ACIS–S measurements and open points indicate ACIS–I measurements. Several trends are seen in Figure 12. First, at 3.5 keV EER(90%) increases linearly between $4-12$ arcmin from about 9 pixels to about 34 pixels. The slopes are similar for the ACIS-I and ACIS-S data, but the ACIS–I spot is systematically smaller at a given off-axis angle compared to the ACIS–S spot. Similar trends are seen for EER(70%), but the spot size is smaller and grows more slowly with radius compared to EER(90%). Although there is less data at 5.2 keV and 6.4 keV, similar trends with radius are seen. Apart from the degraded performance (larger spot size) of the ACIS–S data seen in the 3.5 keV panel of Figure 12, these properties primarily reflect the mirror performance. The degraded off-axis performance of the ACIS-S is roughly as expected from the mismatch between the focal and detector surfaces.

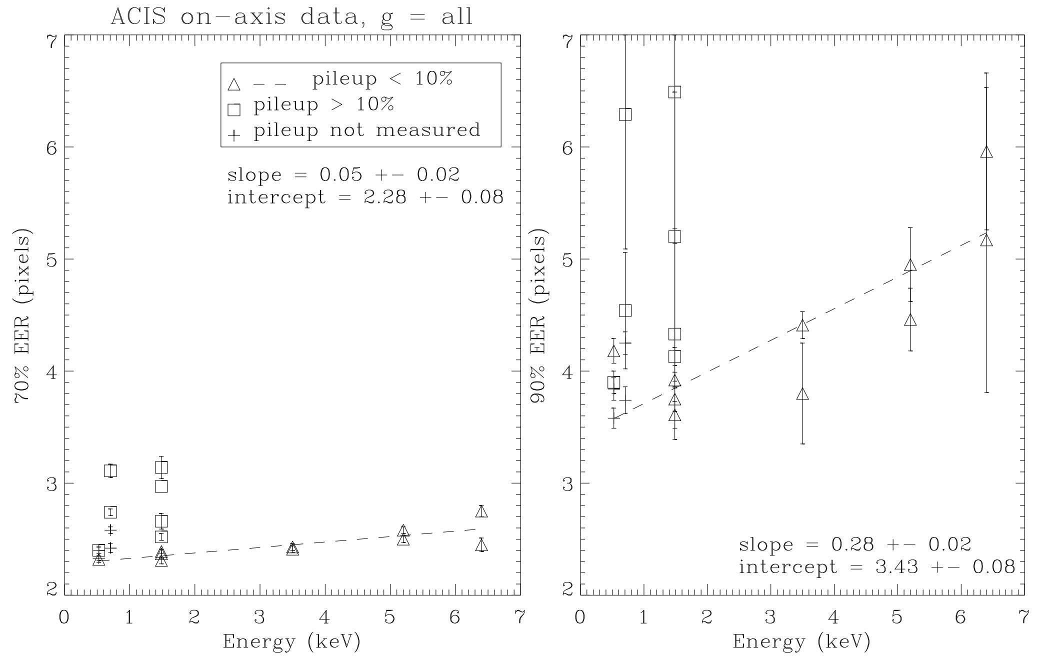

Figure 9: On-axis 70% and 90% encircled energy radii as a function of energy

Table 2: Off-Axis Encircled Energy Radii

Energy (keV)	70%	90%	70%	90%
	ACIS-I		ACIS-S	
3.5	2.18	3.40	2.28	3.45
5.2	1.72	2.59	...	...
6.4	2.87	3.71	...	...

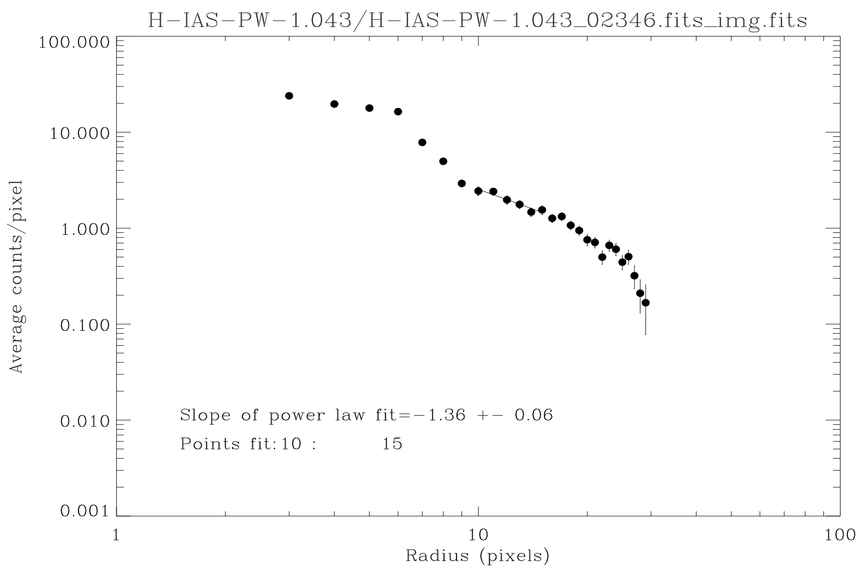

Figure 10: Radial profile of test H–IAS–PW–1.043, showing the least squares linear fit between 10 and 15 pixels

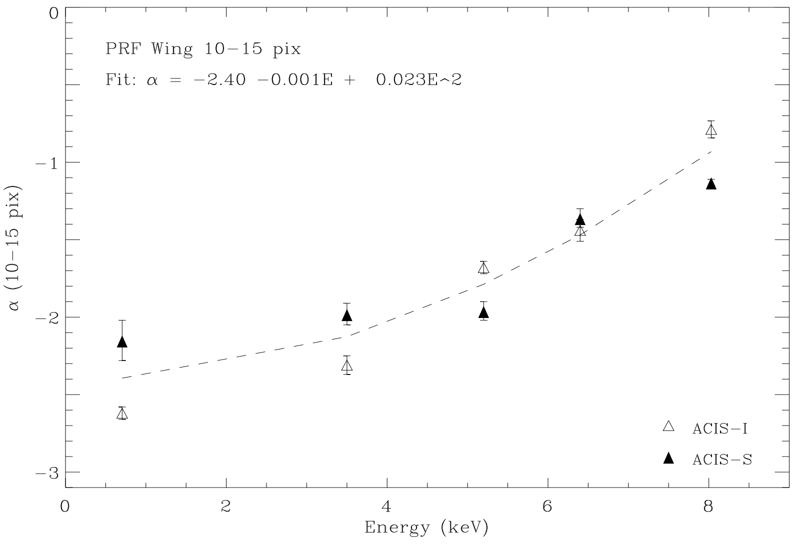

Figure 11: Power law index $\alpha(E)$ for all PRF wing tests

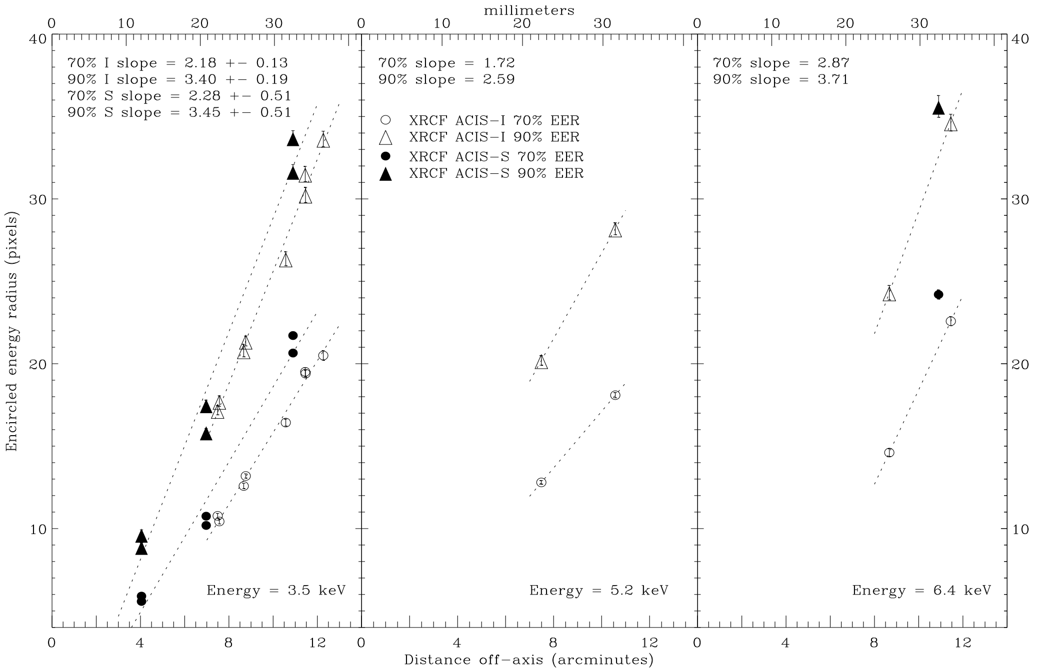

Figure 12: ACIS-I Off-axis 70% and 90% encircled energy radii

7 The Effects of Event Pileup on the Point Response Function

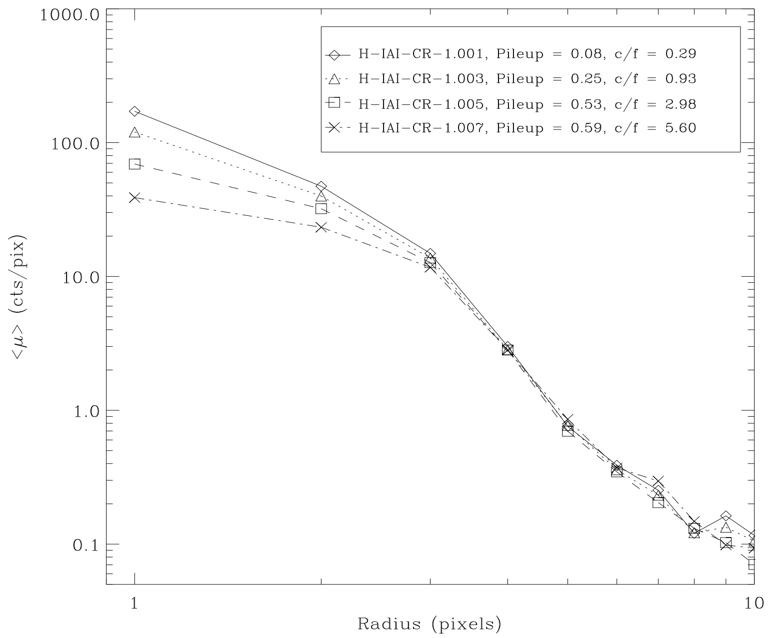

Figure 13: Radial profiles for four pileup cases, normalized between 4 and 6 pixels.

Pileup can be defined as the coincidence of two or more photon events per detection cell per ACIS frame. Pileup signatures appear in both the spatial and spectral information extracted from ACIS, and the strengths of these signatures increase with smaller spot size and larger fluence (counts per frame). In this section we describe the obvious signatures of pileup in the spatial and spectral domains. A further discussion of pileup can be found in

`http://asc.harvard.edu/cal/Links/Acis/acis/Cal_prods/pileup/pileup.html`

7.1 Radial Surface Brightness Profiles

The depression of the spot's central surface brightness relative to the wings with increasing fluence is one of the most obvious pileup signatures in the spatial domain. This effect is shown in Figure 13, where we have plotted the radial surface brightness profiles, normalized at 6 pixels radius, of four on-axis, focussed Al-Kα (1.486 keV) images with fluences ranging from $0.29 - 5.6$ counts per frame. Table 3 lists the XRCF tests, pileup fractions, and fluence for each image. The central surface brightness decreases by more than a factor of four over a factor of 19 in fluence, while the degree of event pileup ranges between $8 - 60\%$. Event pileup fractions are defined as the ratio of the sum of photons in the $n = 2 - 3$ or $n = 2 - 4$ spectral pileup peaks to the total number of photons in the main ($n = 1$) peak plus the pileup peaks calculated as

$$p_p = \frac{\sum\limits_{n>1} A_n \times n}{\sum\limits_{n\geq 1} A_n \times n},$$

where A_n is the area under the main peak or pileup peak.

The surface brightness depression is strongest in the central pixel where the event density is maximal, but the effects migrate to a radius of $\sim$ 4 pixels when the fluence reaches 5.6 cpf. The central depression reflects a deficit of detected events in the core relative to the wings. Because two or more coincident events are counted by the instrument as a single, higher energy event, the number density of counts in the core is reduced with respect to the wings.

7.2 Cumulative Event Distributions

Pileup effects are seen also in the cumulative radial distribution of counts (i.e. the encircled energy). In Figure 14 we show the outward migration of EER(70%) and EER(90%) for these tests. For example, EER(70%) increases from 2.4 pixels for a fluence of 0.29 cpf to 3.1 pixels for a fluence of 5.6 cpf. This effect is again due to central event losses. Similar effects are seen in marginal distributions shown in Figure 15.

Table 3: Pileup data for the four cases shown in Figures 13, 14, 15, and 16.

Image name	Pileup fraction	Counts per frame
H-IAI-CR-1.001	0.08	0.29
H-IAI-CR-1.003	0.25	0.93
H-IAI-CR-1.005	0.53	2.98
H-IAI-CR-1.007	0.59	5.60

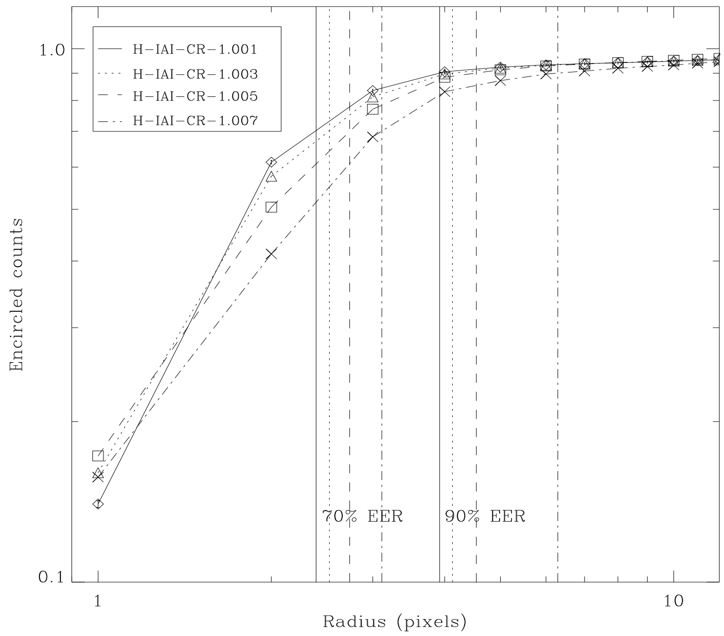

Figure 14: Encircled energy plots for the four pileup cases shown in Figure 13.

7.3 Marginal Distributions

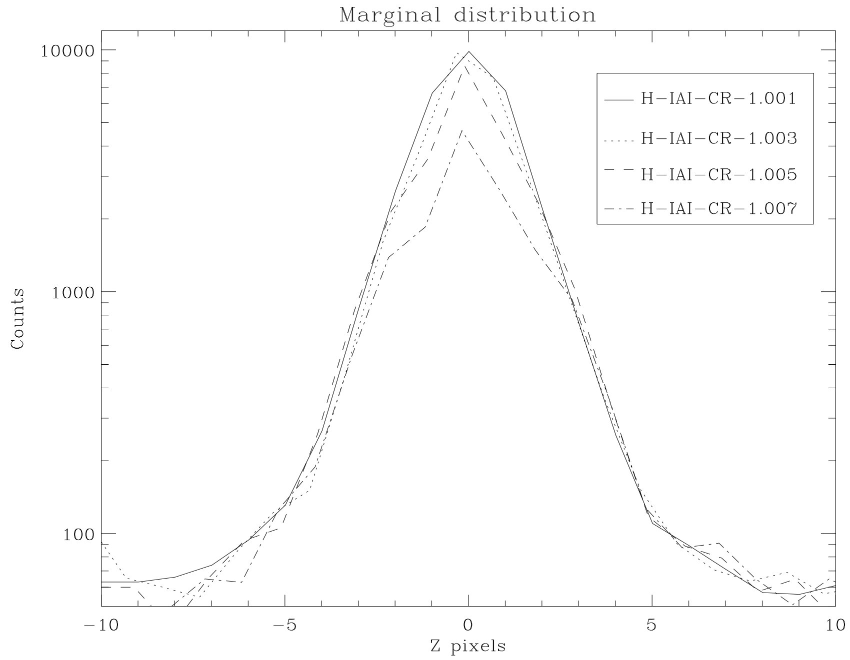

Figure 15: Marginal distributions for the four pileup cases. The profiles were normalized between 5 and 7 pixel radii.

7.4 Orthogonal Slices Through the PRF

In addition to being sensitive to spot asymmetries (e.g. §5.1), image slice profiles are sensitive to pileup when plotted as a function of event grade. In Figure 16, the profile in the Y-direction for all event grades (solid line) is superposed on the profile for standard ASCA grades G02346 (dashed line) for the four images in Figure 13, Figure 14, Figure 15, and Table 3. As the degree of pileup increases, the central surface brightness decreases (c.f. Figure 13, Figure 14), but the effect is more dramatic when including only G02346 event grades. The pileup sensitivity of this grade set is set primarily by migration of grade 0 (single pixel) events into the excluded grade 7. This effect may provide a useful means for diagnosing pileup when the true count rate is unknown. A discussion of this can be found at

`http://asc.harvard.edu/cal/Links/Acis/acis/Cal_prods/pileup/pileup.html`

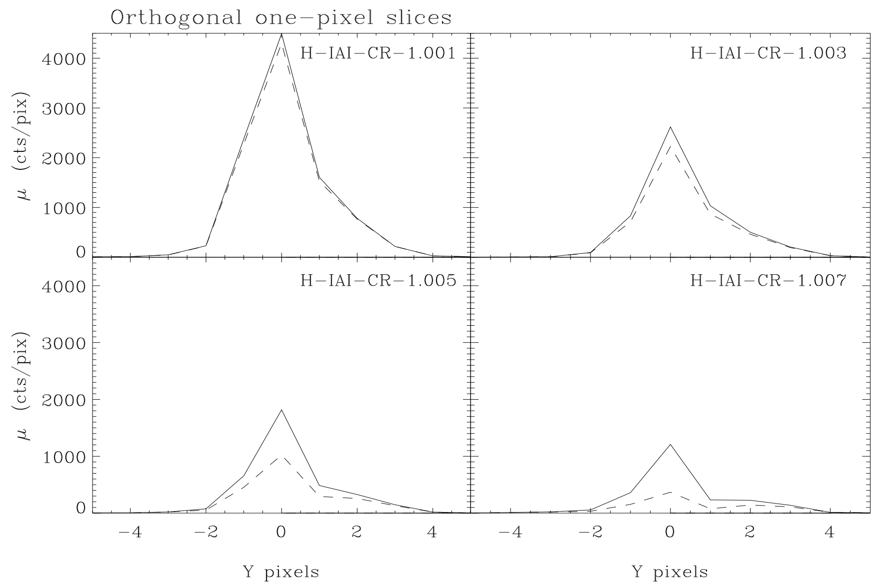

Figure 16: PSF shape: orthogonal slices through the brightest pixel for 4 pileup cases. Dashed lines represent the standard event grades, while solid lines show all grades.

7.5 Pulse Height Spectra

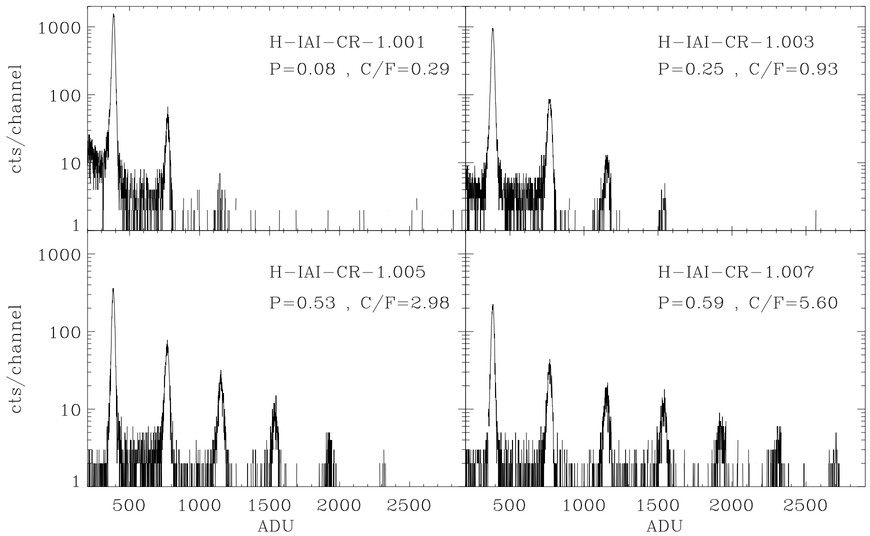

Figure 17: Pulse height spectra of four pileup cases.

Figure 17 shows the pulse height spectra for the four pileup tests. The Al-K line is the largest peak at about 300 ADU and the remaining features are pileup peaks centered at nE ADU. As the degree of pileup increases, the amplitude of the primary peak decreases while the pileup peaks increase in amplitude. The degree of pileup estimated for these and other tests discussed on our web page was found by fitting Gaussians to, and finding the area under, each peak. While the degree of pileup can be determined easily in monochromatic data, it would be difficult for astrophysical objects with realistic spectra.

8 Modeling the PRF Using MARX + SAOSAC

Our principal goal is to provide experimental constraints on the mirror and detector models. We do so by comparing MARX and SAOSAC models to several XRCF images of the core and wings of the HRMA+ACIS X-ray spot. After producing MARX (version 2.14) images with SAOSAC rayfiles with input parameters matching the XRCF tests in question (energy, X-ray flux, axial location, etc.), we analyzed the model and XRCF test data identically. The MARX data were processed using standard MARX analysis tools (e.g. `pileup, marx2fits,` etc.). We are, at present, unable to parse MARX events into ASCA grades, so instead we used AXAF flight event grades. The MARX CCD model does not yet simulate charge trailing due to finite readout time, and does not include a BI device. The SAOSAC model (version xrcf_xss_03) includes the effects of finite source distance, imperfect gravity offloading, and finite source size (for the PRF core tests only).

8.1 PRF Core

Any comparison between model and measurement data is subject to uncertainties in our knowledge of the state of the telescope, most importantly the location of ACIS along the x (defocus) axis. ACIS was shutter focussed at Al-Kα following the pump-down period when

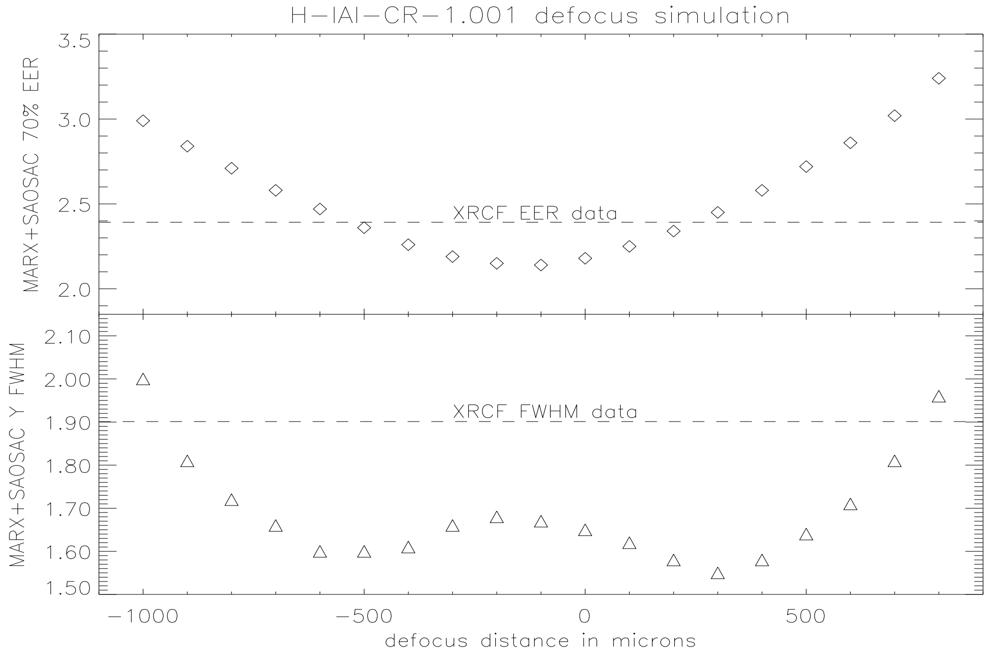

Figure 18: SAOSAC simulations of defocus data for H-IAI-CR-1.001. The horizontal lines represent the XRCF EER(70%) and the FWHM.

Table 4: Encircled Energy radii for XRCF and MARX Data.

Test	Energy (keV)	XRCF EER	MARX EER
H-IAI-PI-1.021	6.4	2.75	2.00
H-IAI-CR-1.001	1.486	2.39	2.12
H-IAI-PI-3.001	1.486	3.15	2.12

the telescope became thermally stable. The focus precision was limited by our ability to measure the relative centroids of the X-ray spot images formed by the HRMA quadrant shutters. Additional focus errors may have accrued by detector drift and by the repeated movement of the five axis mount. The real focus location is not particularly well defined, and this uncertainty must be kept in mind when comparing the data to models.

Our analysis of the PRF core relies heavily on the Al-Kα test H–IAI–CR–1.001, as this is the test with lowest X-ray flux and should suffer the least from the pileup distortions discussed in §7. In Figure 18 we show a plot of the 70% encircled energy radius (top panel) and the FWHM in the y direction (bottom panel) as a function of defocus location for a MARX+SAOSAC model of H–IAI–CR–1.001. The dashed lines in both panels show the measured encircled energy radius and FWHM for the XRCF test. If the HRMA were perfectly focussed and the model were to accurately represent the telescope, the measured EER and FWHM should cross the minimum of each curve. They do not. The model EER is 2.4 pixels while the model minimum is 2.1 pixels, somewhat sharper than the XRCF data. This difference corresponds to a focus offset of ±300 μ in Figure 18. The FWHM simulation is peculiar in that it reaches two minima at roughly ±300 μ. If we assume the central "hump" is image structure and interpolate inward from the wings of the curve, there may be a global minimum that corresponds to the minimum EER and MARX FWHM. We again find that

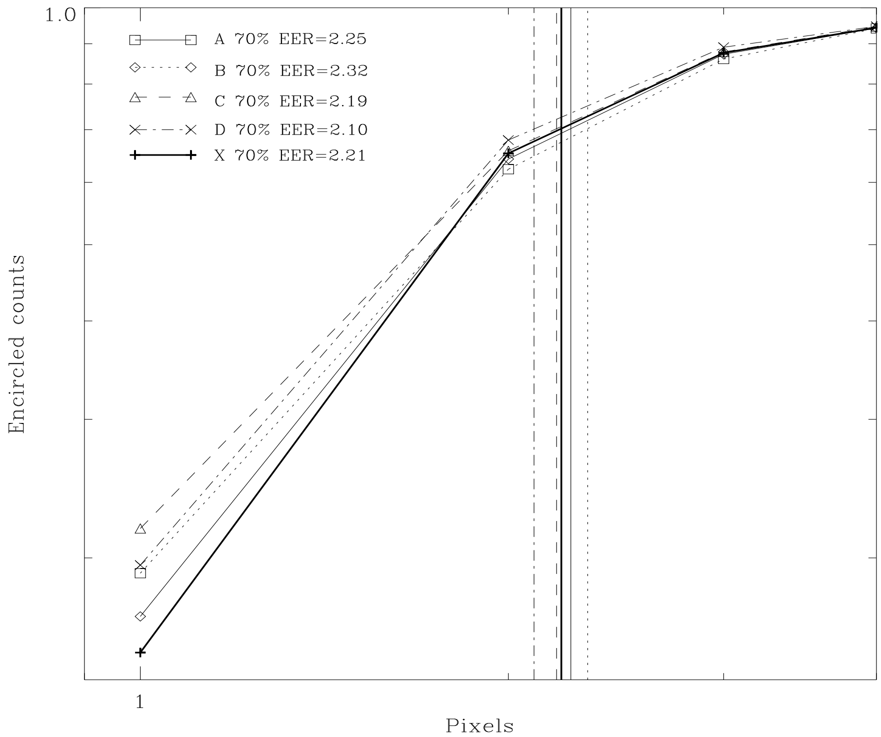

Figure 19: Encircled energy radii for XRCF test H-IAI-CR-1.001 and a set of MARX–SAOSAC simulations, at off-axis positions A=(0.012,0.000), B=(0.012,0.012), C=(0.024,0.012), D=(0.024,0.024).

FWHM of the test data is larger than the model, which would imply a substantial defocus. However, we do not find the same defocus with the EER and FWHM, so we suspect that either the mirror model is too sharp or pixelation effects are throwing off the focus.

We investigate the effects of pixelization in the model by shifting the detector in 12μ steps in orthogonal directions. At each step we used the same SAOSAC raytrace for test H–IAI–CR–1.001 and plotted the cumulative radial distributions and one pixel slices in y through the model and test spots as shown in Figures 19 and 20. The XRCF data in both plots is shown as the thick solid line. The average 70% encircled energy radius and full width for the four realizations of the model is $\langle \mathrm{EER}(70\%) \rangle = 2.14 \pm 0.08$ pixels and $\langle \mathrm{FWHM_y} \rangle = 1.74 \pm 0.14$ pixels.

By comparison, for the XRCF data we find $\langle \mathrm{EER}(70\%) \rangle = 2.21$ and $\langle \mathrm{FWHM_y} \rangle = 1.88$.

The model spot is systematically sharper by 0.07 pixels or $\sim$ 3% in EER(70%) and 0.14 pixels or $\sim$ 7% in FWHM. Although the model again appears to be slightly sharper than the data, the XRCF data are within one standard deviation of the variations due to pixelation. Figure 8 shows a fairly substantial range in the Al-K FWHM (1.5–1.9 pixels) for measurements with modest pileup. Similarly, Figure 9 shows a range in EER(70%) of 2.3–2.4 pixels at Al-K. The sizes of these small variations are on the order of the sizes of pixel structures such as the channel stops and gates on the front side devices, which have lower quantum efficiencies than the active pixel areas. Depending on the location of the spot centroid within a pixel (the images were not dithered) these sub-pixel structures could alter the spot size. Our CCD model makes no attempt to model the gates and channel stops, nor does it handle charge spreading perfectly. We cannot yet determine the relative contributions of the mirror model and detector until the detector model is upgraded, although we note

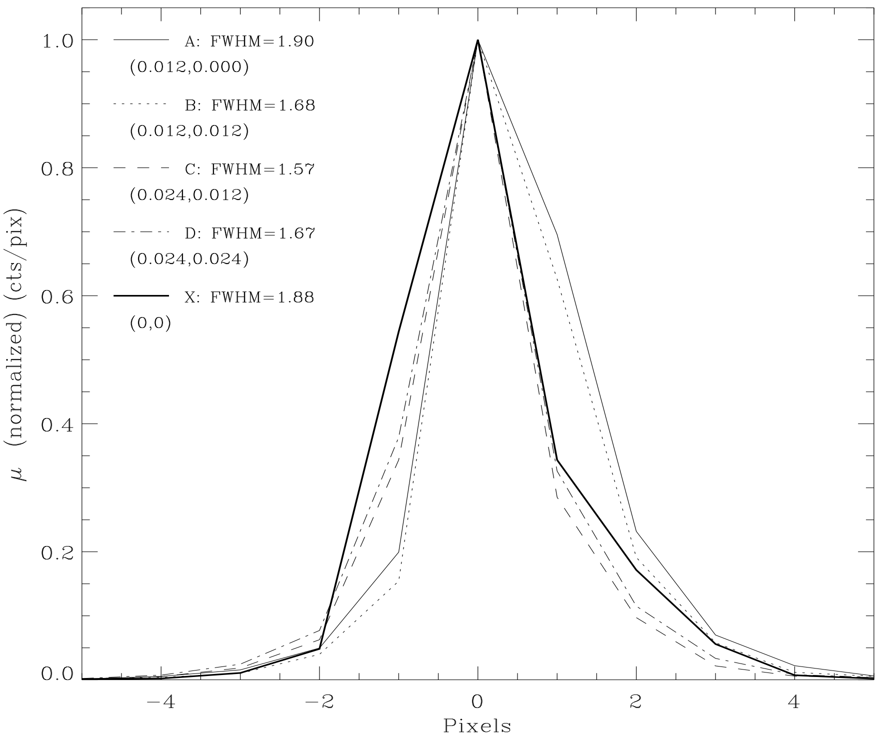

Figure 20: One-pixel slice through MARX–SAOSAC and XRCF images of H-IAI-CR-1.001 test.

following this section that the model spot seems to be slightly smaller than the XRCF spot on all scales.

Table 5: Slopes of fits to off-axis encircled energy radius plots

Energy	Slope			
	XRCF data		MARX data	
	70%	**90%**	**70%**	**90%**
3.5 keV	2.18	3.40	2.39	3.70
5.2 keV	1.72	2.59	2.43	3.41
6.4 keV	2.87	3.71	2.86	4.14

8.2 Comparison to MARX-ACIS Model Spectra

In this section we only briefly point out that the MARX-ACIS model cannot reproduce the degree of pileup in XRCF tests. In Figure 21 we show the PH spectrum for XRCF H-IAI-CR-1.001 (solid line) plotted against three realizations of the SAOSAC+MARX model for the nominal XRCF flux, the flux required to match the counts in the Al-K feature, and the flux required to match the counts in the first pileup peak. This figure and Table 6 show that no incident flux combination can reproduce simultaneously the main peak and pileup peaks. This problem had been encountered in an ongoing effort by McNamara & Wise to develop an algorithm to model pileup in Chandra science observations. However, prior to this point we were unable to determine conclusively the relative contributions of the mirror model and ACIS model to the discrepancy. Now the mirror model looks encouraging, while the detector model appears suspect.

Table 6: Comparison of MARX+SAOSAC Spectra to XRCF Spectra

Data	BND Flux	Pileup	Peak
	p cm^{-2} s^{-1}	(event)	(cts/chan)
H-IAI-CR-1.001	0.00452	0.080	1499
MARX	0.00452	0.136	1297
MARX, flux+15%	0.00520	0.157	1445
MARX, flux−20%	0.00362	0.112	1074
MARX, flux−40%	0.00271	0.084	834

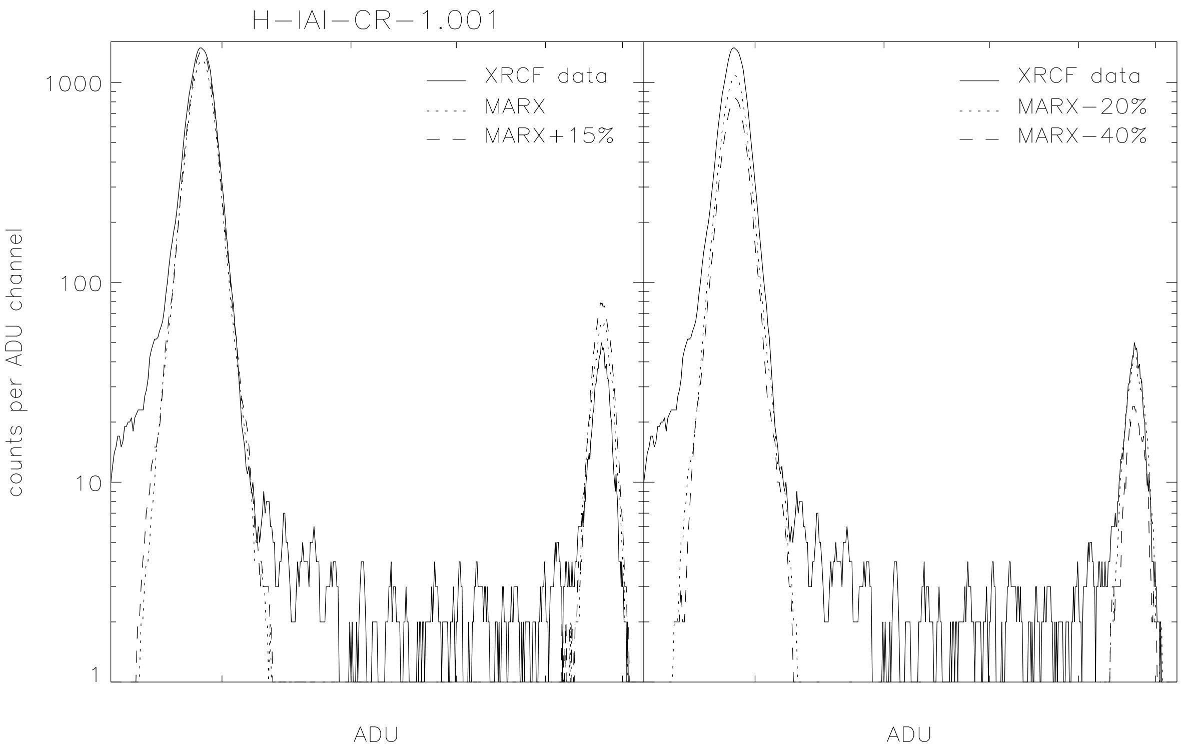

Figure 21: Comparison between ACIS-I spectrum of H-IAI-CR-1.001 and MARX pileup simulations.

8.3 Model Comparison to Off-Axis Images

In this section we briefly compare the properties of the PRF wings discussed in §5.2 and the off-axis PRF discussed in §6 to MARX+SAOSAC models. The modeled and measured data were analyzed in the same way and plotted in Figure 22, showing the 70% and 90% EER at three energies (3.5 keV, 5.2 keV, 6.4 keV) and at several off-axis angles. (At the time of these simulations, finite source size models were unavailable. However, we should be insensitive to finite source size effects at these off-axis angles.)

Several trends are seen in Figure 22 between EER and off-axis location at all energies. First, EER(90%) increases faster with radius than the EER(70%) (slopes and errors are given in Figure 22). Second, the slopes derived from the MARX+SAOSAC model agree fairly well with the XRCF data. Third, although the slopes agree, the models appear to be tighter than the XRCF data by $\lesssim$ 10%. The slope differences between EER(70%) and EER(90%) are produced by mirror scattering. However, we do not understand the systematically smaller model spot size, although we can exclude pixelization on these scales.

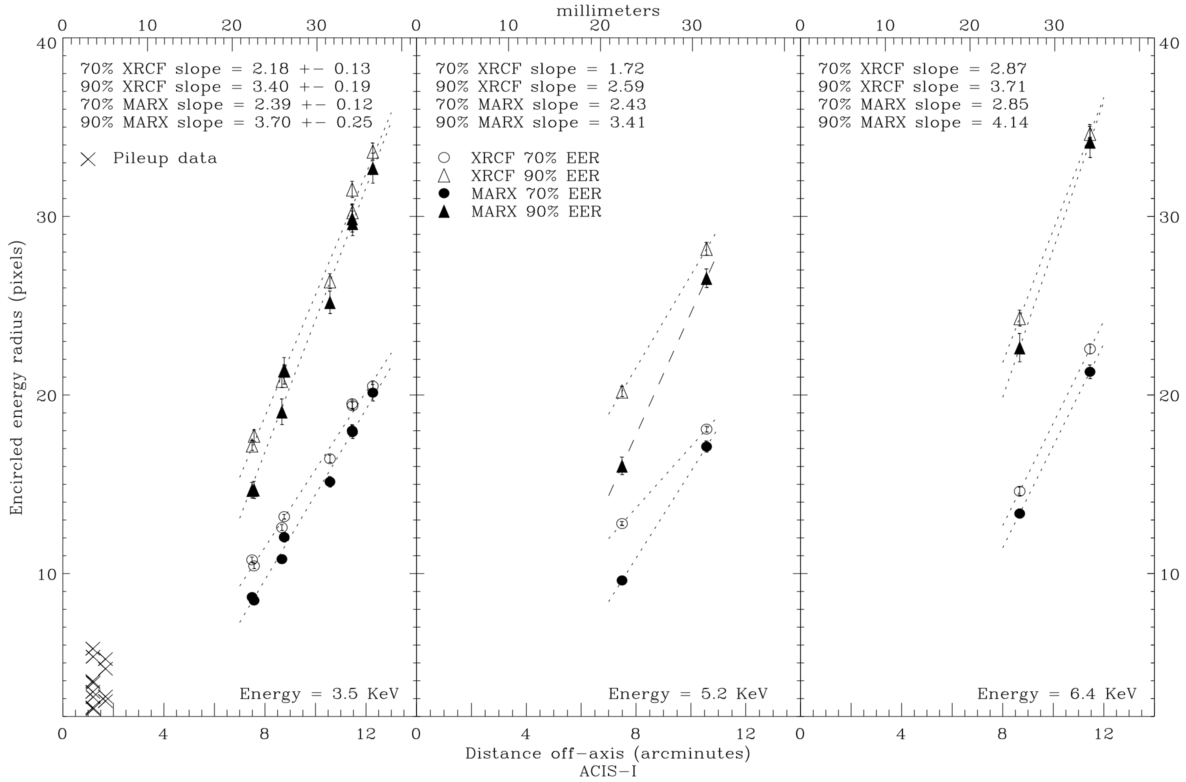

Figure 22: ACIS-I XRCF and SAOSAC-MARX data: off-axis 70% and 90% encircled energy radii.

All of the analysis products are available online at
`http://asc.harvard.edu/cal/Links/Acis/acis/Cal_prods/psf/psf.html`

9 Summary

We presented relationships between the ACIS-XRCF spot size and PRF shape as a function of energy, off-axis angle, and degree of pileup (fluence), and we compared these relationships to the SAOSAC+ACIS model as implemented in MARX. We arrived at the following conclusions.

• The SAOSAC+MARX model FWHM and EER(70%) are within a few percent of XRCF Al-K on-axis data, and are within one standard deviation of the scatter in these quantities imparted by ACIS pixelation.

• The off-axis model spot is slightly smaller than the XRCF spot at all energies and off-axis angles, but the modeled growth of the spot with increasing off-axis angle agrees with the data to within the measurement errors.

• The current MARX–ACIS model cannot reproduce observed XRCF pileup spectra for any reasonable range of model parameters. This limits the current ACIS model's utility for modeling Chandra science spectra. The new MIT model will soon be implemented into MARX and this issue will be revisited.

• The ACIS model itself is apparently the limiting factor in our ability to model the on-orbit performance of Chandra.

• We have prepared a web site containing data and detailed analyses for most of the in-focus, XRCF Phase H ACIS tests. The data and information contained at this site are intended for detailed comparisons to the telescope model and on-orbit calibration data, and to aid in software development.

`http://asc.harvard.edu/cal/Links/Acis/acis/Cal_prods/psf/psf.html`

Future work:

• Install new MIT ACIS model currently being used to generate ACIS response matrices into MARX, and repeat raytrace simulations for a larger sample of tests. The new model, with a presumably improved gate structure and more realistic quantum efficiency, should provide a better understanding of pixelation effects and hopefully a more robust pileup treatment

• Produce backside chip simulations when model becomes available

• Continue efforts to calibrate MARX as an analysis tool

We are indebted to Diab Jerius for providing the SAOSAC rays used in this analysis, and for implementing the finite source size model into SAOSAC. We thank Dick Edgar, Terry Gaetz, Mike Wise, and Kester Allen for their help and advice.

Test Data

Test	Energy	BND flux	Framesize	FT	Photon pileup		Event pileup	
	keV	p cm^{-2} s^{-1}	pix	s	All	Std.	All	Std.
On-axis PSF								
H-IAI-PI-1.021	6.400	0.0246 ± 0.0018	38 × 1024	0.122	0.098	0.085	0.051	0.044
H-IAI-PI-1.023	0.705	0.0387 ± 0.0035	38 × 1024	0.122	...	...	...	...
H-IAI-PI-12.001	8.030	0.1256 ± 0.0092	38 × 1024	0.122	...	...	...	...
H-IAI-PI-2.019	3.500	0.0134 ± 0.0015	38 × 1024	0.122	0.099	0.093	0.052	0.049
H-IAI-PI-3.001	1.486	0.0199 ± 0.0014	100 × 1024	0.8	0.576	0.445	0.340	0.240
H-IAI-PI-2.022	5.200	0.0215 ± 0.0020	38 × 1024	0.122	0.158	0.140	0.082	0.072
H-IAS-PI-1.041	6.400	[0.04]	38 × 1024	0.122	0.057	0.043	0.029	0.022
H-IAS-PI-1.042	0.705	[0.01]	38 × 1024	0.122	...	...	...	...
H-IAS-PI-12.002	8.030	[0.14]	38 × 1024	0.122	0.093	0.072	0.049	0.037
H-IAS-PI-2.043	3.500	[0.01]	38 × 1024	0.122	0.100	0.079	0.052	0.041
H-IAS-PI-2.044	5.200	[0.02]	38 × 1024	0.122	0.158	0.129	0.082	0.066
On-axis PSF wing tests								
H-IAI-PW-1.025	6.400	[1.3]	38 × 1024	0.122	...	...	...	...
H-IAI-PW-1.027	0.705	[1.6]	38 × 1024	0.122	...	...	...	...
H-IAI-PW-2.025	3.500	[0.46]	38 × 1024	0.122	...	...	...	...
H-IAI-PW-12.003	8.030	[5.2]	38 × 1024	0.122	...	...	...	...
H-IAI-PW-2.028	5.200	[1.9]	38 × 1024	0.122	...	...	...	...
H-IAS-PW-1.043	6.400	[1.2]	38 × 1024	0.122	...	...	...	...
H-IAS-PW-1.044	0.705	[0.31]	38 × 1024	0.122	...	...	...	...
H-IAS-PW-12.004	8.030	[4.6]	38 × 1024	0.122	...	...	...	...
H-IAS-PW-2.045	3.500	[0.46]	38 × 1024	0.122	...	...	...	...
H-IAS-PW-2.046	5.200	[2.1]	38 × 1024	0.122	...	...	...	...
Pileup tests								
H-IAI-CR-1.001	1.486	0.0045 ± 0.0005	38 × 1024	0.122	0.080	0.071	0.041	0.037
H-IAI-CR-1.003	1.486	0.0167 ± 0.0008	38 × 1024	0.122	0.245	0.230	0.132	0.124
H-IAI-CR-1.005	1.486	0.0544 ± 0.0010	38 × 1024	0.122	0.534	0.469	0.313	0.264
H-IAI-CR-1.007	1.486	0.1038 ± 0.0058	38 × 1024	0.122	0.589	0.438	0.344	0.232
H-IAI-CR-1.009	0.525	0.0247 ± 0.0048	38 × 1024	0.122	0.125	0.104	0.067	0.055
H-IAI-CR-1.011	0.525	0.0712 ± 0.0082	38 × 1024	0.122	0.266	0.243	0.143	0.130
H-IAS-CR-1.002	1.486	0.0039 ± 0.0003	38 × 1024	0.122	0.064	0.051	0.033	0.026
H-IAS-CR-1.004	1.486	0.0127 ± 0.0008	38 × 1024	0.122	0.231	0.186	0.123	0.098
H-IAS-CR-1.006	1.486	0.0435 ± 0.0023	38 × 1024	0.122	0.548	0.395	0.319	0.212
H-IAS-CR-1.008	1.486	0.0825 ± 0.0067	38 × 1024	0.122	0.626	0.369	0.372	0.182
H-IAS-CR-1.010	0.525	0.0312 ± 0.0041	38 × 1024	0.122	...	...	...	...
H-IAS-CR-1.012	0.525	[0.02]	38 × 1024	0.122	...	...	...	...

Figure 23: Energy, BND flux, framesize, frametime, and pileup fractions for all on-axis XRCF tests used in our analysis of the ACIS PRF.

Off-axis PSF

Test	Energy	BND flux	Framesize	FT	Photon pileup		Event pileup		Pitch	Yaw	Defocus
	keV	p cm^{-2} s^{-1}	pix	s	All	Std.	All	Std.	arcmin		mm
H-IAI-PI-2.013	3.500	[0.0078]	38 × 1024	0.8	0.304	0.258	0.179	0.148	0	1.19	+0
H-IAI-PI-2.007	3.500	[0.0078]	38 × 1024	0.8	0.305	0.263	0.180	0.151	1.2	0	+0
H-IAI-PI-2.001	3.500	[0.0078]	38 × 1024	0.8	0.303	0.268	0.179	0.155	1.2	1.19	+0.001
H-IAI-PI-2.009	3.500	[0.0078]	100 × 1024	0.5	...	...	...	...	1.22	-7.47	+0.024
H-IAI-PI-2.003	3.500	[0.0078]	38 × 1024	0.8	...	...	...	...	8.68	1.19	+0.032
H-IAI-PI-2.002	3.500	[0.0095]	100 × 1024	0.5	...	...	...	...	8.68	8.67	+0.063
H-IAI-PI-1.005	6.400	[0.0961]	100 × 1024	0.5	...	...	...	...	8.68	-7.47	+0.054
H-IAI-PI-2.008	3.500	[0.0078]	38 × 1024	0.8	...	...	...	...	8.68	-7.47	+0.054
H-IAI-PI-1.014	6.400	[0.0779]	100 × 1024	0.5	...	...	...	...	-0.02	8.67	+0.031
H-IAI-PI-2.015	3.500	[0.0078]	100 × 1024	0.5	...	...	...	...	-0.02	8.67	+0.031
H-IAI-PI-2.020	3.500	[0.0095]	100 × 1024	0.5	...	...	...	...	-7.48	-7.47	+0.046
H-IAI-PI-2.023	5.200	[0.0272]	100 × 1024	0.5	...	...	...	...	-7.48	-7.47	+0.046
H-IAI-PI-2.021	3.500	[0.0078]	38 × 1024	0.8	...	...	...	...	-7.49	0	+0.023
H-IAI-PI-2.024	5.200	[0.0245]	38 × 1024	0.8	...	...	...	...	-7.49	0	+0.023
H-IAI-PI-3.003	1.486	[0.0095]	38 × 1024	0.8	...	...	...	...	-7.49	0	+0.023
H-IAI-PI-3.006	1.486	[0.3662]	38 × 1024	0.8	0.348	0.273	0.191	0.146	-7.49	0	+0.023
H-IAI-PI-2.014	3.500	[0.0095]	100 × 1024	0.5	...	...	...	...	-7.49	8.68	+0.055
H-IAI-PI-7.002	1.486	[0.01]	100 × 1024	0.5	...	...	...	...	-7.49	-7.49	+0
H-IAI-PI-7.005	1.486	[0.41]	100 × 1024	0.5	0.186	0.158	0.103	0.086	-7.49	-7.49	+0
H-IAI-PI-2.035	3.500	[0.0078]	38 × 1024	0.8	...	...	...	...	3.73	1.57	+0.006
H-IAS-PI-3.008	1.486	[0.0071]	38 × 1024	0.8	...	...	...	...	3.73	1.57	+0.006
H-IAS-PI-3.013	1.486	[0.2812]	38 × 1024	0.8	...	...	...	...	3.73	1.57	+0.006
H-IAS-PI-2.032	3.500	[0.0095]	38 × 1024	0.8	...	...	...	...	3.73	10.24	+0.049
H-IAS-PI-2.036	3.500	[0.0078]	38 × 1024	0.8	...	...	...	...	3.73	-5.89	+0.02
H-IAS-PI-3.009	1.486	[0.0077]	38 × 1024	0.8	...	...	...	...	3.73	-5.89	+0.02
H-IAS-PI-3.014	1.486	[0.2812]	38 × 1024	0.8	...	...	...	...	3.73	-5.89	+0.02
H-IAS-PI-7.010	1.486	[0.0071]	100 × 1024	0.5	...	...	...	...	-3.7	1.6	+0
H-IAS-PI-7.015	1.486	[0.2812]	100 × 1024	0.5	...	...	...	...	-3.7	1.6	+0
H-IAS-PI-7.011	1.486	[0.0077]	100 × 1024	0.5	...	...	...	...	-3.7	-5.9	+0
H-IAS-PI-7.016	1.486	[0.2812]	100 × 1024	0.5	...	...	...	...	-3.7	-5.9	+0
H-IAS-PI-2.037	3.500	[0.0078]	100 × 1024	0.5	...	...	...	...	-3.73	1.57	+0.006
H-IAS-PI-2.038	3.500	[0.0078]	100 × 1024	0.5	...	...	...	...	-3.73	-5.89	+0.02
H-IAS-PI-1.029	6.400	[0.0865]	100 × 1024	0.5	...	...	...	...	-3.73	10.24	+0.049
H-IAS-PI-2.031	3.500	[0.0095]	100 × 1024	0.5	...	...	...	...	-3.73	10.24	+0.049

Figure 24: Energy, BND flux, framesize, frametime, and pileup fractions for all off-axis XRCF tests used in our analysis of the ACIS PRF.

The ACIS PSF Calibration Website

Note: This website was designed with Netscape Communicator 4.5, and may look slightly different with other browsers.

The ACIS Calibration Data and Data Products website provides access to all ACIS calibration data, and is located at:

`http://asc.harvard.edu/cal/Links/Acis/acis/WWWacis_cal.html`

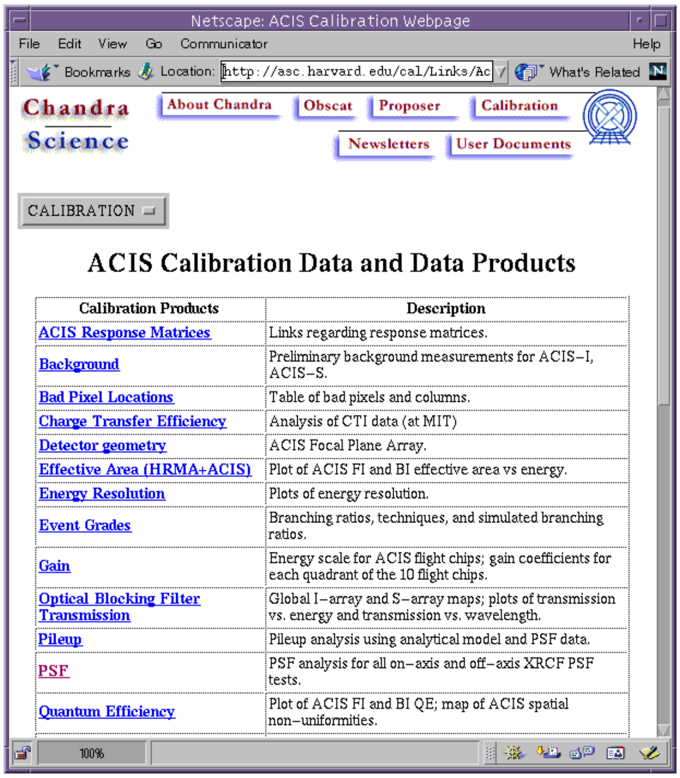

Figure 25: The front page of the ACIS PSF Calibration Data and Data Products website.

Clicking on any of the calibration products listed in the table will open a new topic page. Links are provided for related calibration data and other topics of interest, such as the ACIS Team Calibration Report and the PSU and MIT ACIS sites.

To open the main PSF calibration page, click on the “PSF” link in the Calibration Products column, or open:

`http://asc.harvard.edu/cal/Links/Acis/acis/Cal_prods/psf/psf.html`

The PSF Calibration Page

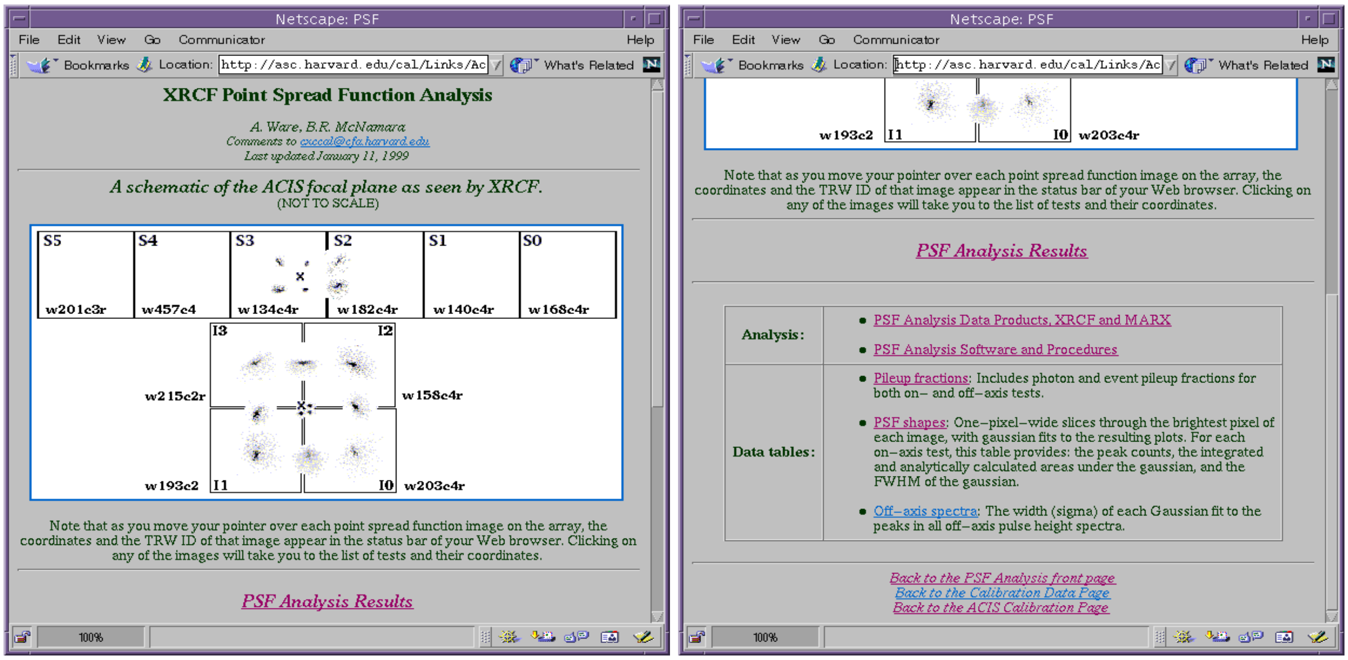

Figure 26: The PSF Calibration Page

The main PSF page contains three sections: a schematic of the ACIS focal plane, a link to the PSF analysis results, and a table of other links. These sections are summarized below.

- *Schematic of the ACIS focal plane:* As you move the mouse pointer over the images, the status bar (at the bottom of the browser window) will display the off-axis distance in arcminutes, as well as the name of the test pictured. Clicking on an image will open the list of data products for that location on the detector. Each chip is labeled with its serial number, and the X on chips I3 and S3 marks each array's aimpoint.
- *PSF Analysis Results:* This page (shown in Figure 27) contains analyses including the encircled energy radius, radial profiles, and orthogonal one pixel wide slices, for on- and off-axis XRCF and MARX+SAOSAC data. Clicking on any of the images on this page will open the page containing the analysis. Plots on most of these analysis pages have been converted to "clickable imagemaps":
  - moving the mouse pointer over any data point on the plot will display the test ID and Y-value of that point in the status bar
  - clicking on a data point will open a Postscript file containing the appropriate analysis product, e.g. if you click on a point in the "70% Encircled energy vs. energy" plot, your computer will display the encircled counts vs. radius plot with which that 70% encircled energy was measured.
- *Table of other links:* In the Analysis section, "PSF Analysis Data Products" contains links to data products organized by test ID and type, and "PSF Analysis Software and Procedures" is a guide to using the software written to generate the analysis products. The links to the data tables are fairly self-explanatory. The tables are all in HTML

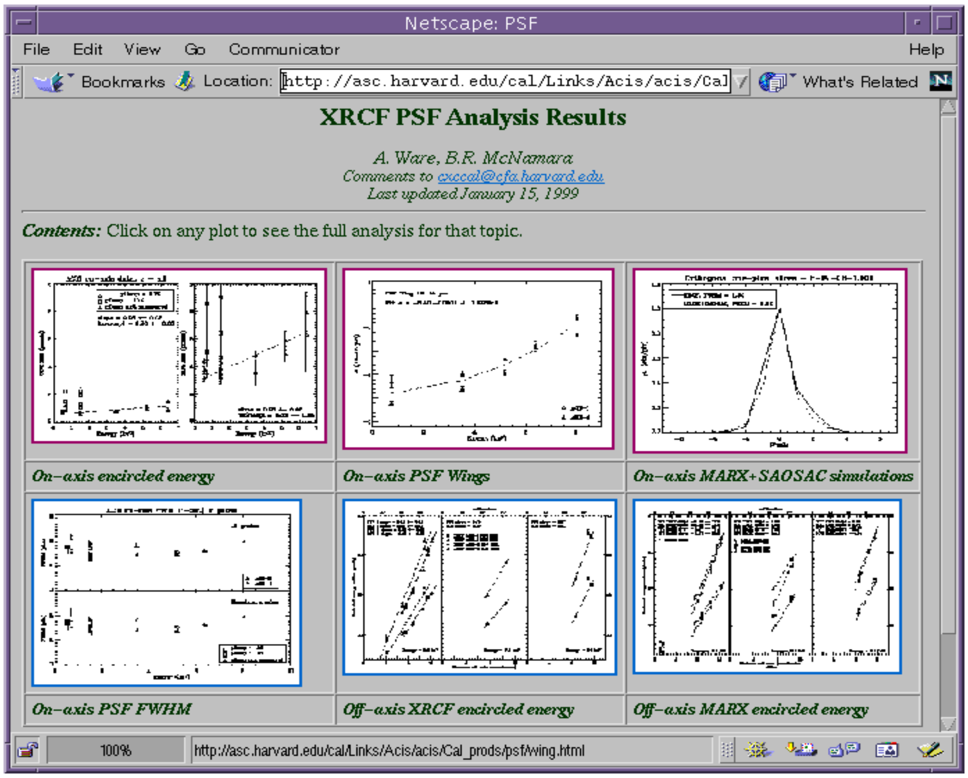

Figure 27: PSF Analysis Results

format. The data tables generally contain links to relevant data products organized by test TRWID.

Questions about any part of the CXC calibration website should be emailed to *cxccal@cfa.harvard.edu*.